Icarus 202 (2009) 240–248

Contents lists available at ScienceDirect

Icarus

www.elsevier.com/locate/icarus

Saturn's south polar vortex compared to other large vortices in the Solar System

Ulyana A. Dyudina [a,*], Andrew P. Ingersoll [a], Shawn P. Ewald [a], Ashwin R. Vasavada [b], Robert A. West [b], Kevin H. Baines [b], Thomas W. Momary [b], Anthony D. Del Genio [c], John M. Barbara [c], Carolyn C. Porco [d], Richard K. Achterberg [e], F. Michael Flasar [e], Amy A. Simon-Miller [e], Leigh N. Fletcher [b]

[a] Division of Geological and Planetary Sciences, 150-21, California Institute of Technology, Pasadena, CA 91125, USA
[b] Jet Propulsion Laboratory, California Institute of Technology, Pasadena, CA 91109, USA
[c] Goddard Institute for Space Studies, NASA, 2880 Broadway, New York, NY 10025, USA
[d] Cassini Imaging Central Laboratory for Operations, Space Science Institute, 4750 Walnut Street, Suite 205, Boulder, CO 80301, USA
[e] NASA Goddard Space Flight Center, Code 693, Greenbelt, MD 20771, USA

ARTICLE INFO

Article history:
Received 19 September 2008
Revised 9 February 2009
Accepted 15 February 2009
Available online 26 February 2009

Keywords:
Saturn, atmosphere
Atmospheres, dynamics
Infrared observations
Meteorology
Spectroscopy

ABSTRACT

Observations made by the Imaging Science Subsystem (ISS), Visible and Infrared Mapping Spectrometer (VIMS) and the long-wavelength Composite Infrared Spectrometer (CIRS) aboard the Cassini spacecraft reveal that the large, long-lived cyclonic vortex at Saturn's south pole has a 4200-km-diameter cloud-free nearly circular region. This region has a 4 K warm core extending from the troposphere into the stratosphere, concentric cloud walls extending 20–70 km above the internal clouds, and numerous external clouds whose anticyclonic vorticity suggests a convective origin. The rotation speeds of the vortex reach 150 ± 20 m s^{-1}. The Saturn polar vortex has features in common with terrestrial hurricanes and with the Venus polar vortex. Neptune and other giant planets may also have strong polar vortices.

1. Introduction

Earth-based telescopic observations of 2003 (Orton and Yanamandra-Fisher, 2005) revealed a hot spot at Saturn's south pole, which was observed again by Cassini composite infrared spectrometer (CIRS) (Fletcher et al., 2008). Cassini imaging observations (Vasavada et al., 2006; Sánchez-Lavega et al., 2006) revealed cyclonic rotation around the spot in 2005. To explore this feature further, a series of high-resolution observations by Cassini were taken for a 3-hour period on October 11, 2006. This observation revealed that the hot spot is surrounded by the double cloud wall. We call this structure an "eye" of the vortex because it displays some similarities with an eye of a terrestrial hurricane, as we discuss in Section 8. The eye has nearly cloud-free upper atmosphere above lower, tropospheric clouds. The eye is bordered by two 20–70-km-tall cloud walls. The eye is surrounded by the ring of high hazes (Dyudina et al., 2008).

In this paper we provide a detailed description and discussion of the October 11, 2006 imaging observations of the cyclone which were published as Science breves by Dyudina et al. (2008). Additionally we present simultaneous observations of the vortex by two other instruments: high-resolution infrared CIRS maps and 5-micron VIMS movies of the Saturn's south polar vortex (SPV). With this data we compare SPV with large atmospheric vortices on Earth, Venus, Jupiter, and Neptune.

Section 2 discusses morphology of the clouds and their vertical structure. Section 3 presents our wind speed measurements. Section 4 shows the vorticity of the wind. Section 5 discusses the heights of the two cloud walls around the polar storm's eye. Section 6 describes the hot spot at the location of SPV observed by Cassini CIRS. Section 7 compares our windspeed measurements with Cassini VIMS wind measurements. Section 8 compares SPV with large vortices on other planets.

2. Cloud structure

On October 11, 2006 Cassini ISS observed the south pole of Saturn from an orbital distance of 5.6 Saturn radii with unprecedented spatial resolution of 20 km/pixel. The Sun was about 15° above the horizon and the spacecraft was about 40° above the horizon at the pole. The camera took a multiple-filter set of images each covering the polar area within the −80° latitude circle. Parts of the images covered latitudes as low as −70°.

Fig. 1 shows a mosaic from 14 images of the south pole taken within a 3-hour period. The two walls of the cyclone are the circular structure at around −87.8° latitude and the slightly elliptical structure at around −88.7° to −88.9° latitude. The same double-wall structure apparently existed during the ~50 km/pixel Cassini

* Corresponding author. Fax: +1 (626) 585 1917.
E-mail address: ulyana@gps.caltech.edu (U.A. Dyudina).

0019-1035/$ – see front matter
doi:10.1016/j.icarus.2009.02.014

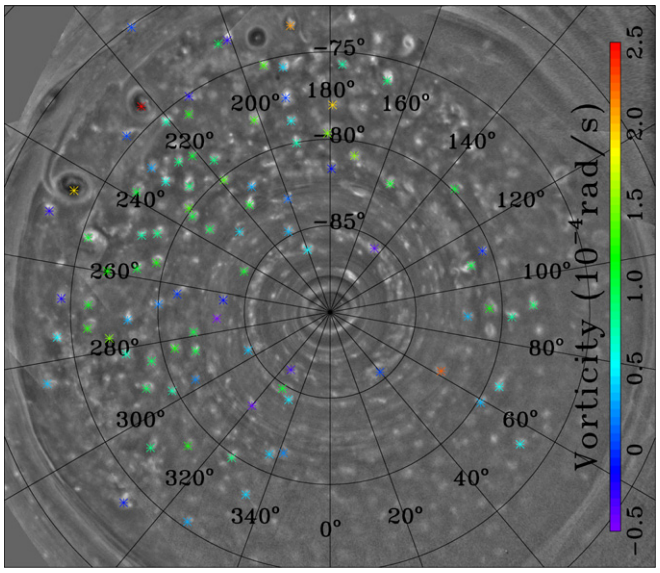

Fig. 1. Map of the SPV combined as a mosaic of 14 maps produced from individual ISS images. Each image was taken in continuum band filter CB2 with the central wavelength 750 nm (Porco et al., 2004). To reduce the effect of varying solar illumination across the image, each image is high-pass filtered at the spatial scale of ∼200 km, or ∼0.2° latitude. The map is labeled by the west longitude and planetocentric latitude. Asterisks show locations of the individual features for which vorticity has been measured. The value of the vorticity is indicated by the asterisks' color. The vorticity data are also plotted in Fig. 2B. (For interpretation of the references to color in this figure legend, the reader is referred to the web version of this article.)

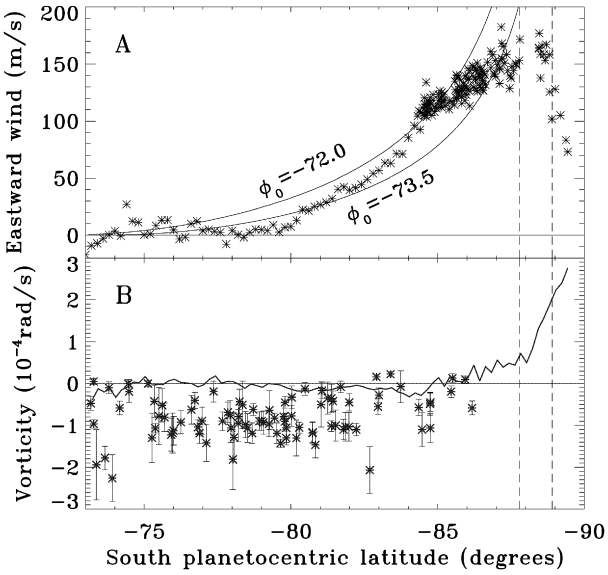

Fig. 2. Profiles of zonal velocity (eastward) and cyclonic vorticity (clockwise) around Saturn's south pole. The dashed vertical lines indicate the inner and outer eyewalls. (A) Zonal velocity measured by tracking clouds in a sequence of images over a 3-hour period. The asterisks indicate data points taken from automatic tracking at latitudes equatorward from 84.5° S, or from manual feature tracking at latitudes poleward from 84.5° S. The solid curves are for constant absolute vorticity $\zeta + f$ starting at latitude ϕ_0 (values labeled on the curves) with $\bar{u} = 0$ and $\zeta = 0$ at that point. (B) Relative vorticity ζ. The solid curve is a spline fit to the velocity data of Fig. 2A. The points are the small white clouds of Fig. 1 marked by asterisks.

polar observations taken in September–October 2004, two years earlier (Vasavada et al., 2006), and in the ∼30 km/pixel observations taken in July 2004 (Sánchez-Lavega et al., 2006). However with lower spatial resolution, slant viewing, and higher Sun producing shorter shadows, the 2004 observations were incapable of detecting the steep eyewalls. The elliptical shape of the inner eyewall looks remarkably unchanged between the 2004 and 2006 observations. There are a few small clouds inside the inner eyewall and many small bright clouds surrounding the eye that have the same general appearance between 2004 and 2006 observations.

From the imaging in wavelengths sensitive to different altitudes, Dyudina et al. (2008) concluded that the "eye" of the vortex is cloud-free in the upper troposphere, and that the small bright clouds both inside and outside the eye are located in the lower troposphere (see also the description of cloud height retrieval in Section 3 of this paper).

3. Windspeeds

Cassini took repeated images of the pole during the 3-hour observation. High spatial resolution of ∼20 km/pixel and good temporal sampling of 14 images in the continuum band filter at 750 nm (the wavelength of the best contrast for small features) allowed tracking of clouds to obtain accurate wind velocities. The supplementary online movie 1combined from these images shows the winds increasing toward the pole. The cyclone's eye rotates by ∼60° relative to the planet within the 3 hours. Fig. 2A shows zonal windspeeds measured by cloud tracking in the Voyager System III longitude system, which was defined by the Voyager-era Saturn Kilometric Radiation rotation period of $10^h39^m24^s$ (Desch and Kaiser, 1981). Two tracking techniques were used. Equatorward of −84.5° latitude the windspeeds were obtained by an automatic feature tracker. Poleward of −84.5° latitude the automatic tracker failed to obtain accurate wind speeds because of high speeds, curved trajectories, and multiple linear cloud features. For this region we manually tracked individual features using modified movies combined from the 14 maps. In each modified movie the maps were rotated back relative to the clouds' zonal motion at some test angular velocity around the pole. For each cloud there is a particular angular velocity when the cloud's zonal motion and the movie's back rotation cancel out, which stops the motion of the cloud. From the set of test angular velocities we picked the clouds that stopped their motion in the modified movies. This produced the data points in Fig. 2A.

The manual and automatic tracking agree equatorward from −84.5° latitude. The independent cloud tracking by two other coauthors (J.M.B. and A.R.V.) agree with the windspeeds in Fig. 2A but have larger uncertainties. We do not include their data points in Fig. 2A. The wind increases toward the pole up to the outer eyewall at −87.8° latitude. There are no trackable features between the outer wall and latitude of −88.5°, which is just outside the inner eyewall. Between latitudes −86.5° and −89° the mean zonal velocity $\bar{u}$ reaches its maximum of 150 ± 20 m s^{-1}.

The winds measured using Cassini images taken in July 2004 were 160 ± 10 m/s at −87° latitude (Sánchez-Lavega et al., 2006). This is consistent with our measurements at this latitude. In September–October 2004 the speed of rotation of the inner eyewall at −88.5° latitude was 80 to 135 m/s (Vasavada et al., 2006). This is smaller than our $\bar{u} = 150 \pm 20$ m s^{-1} for this latitude (see Fig. 2A). Although this difference may be real, the uncertainty in the lower resolution Vasavada et al. (2006) windspeed measurements does not allow us to claim a windspeed change with confidence.

The smooth curves in Fig. 2A assume constant absolute vorticity poleward of latitude ϕ_0. Absolute vorticity is related to spin about a vertical axis and consists of two parts – a part ζ due to motion relative to the planet and a part f due to the planet's rotation. The curves assume $\zeta + f = f_0 =$ constant, with $\zeta = 0$ and $\bar{u} = 0$ at $\phi = \phi_0$. The latitude ϕ_0 is the only free parameter of the curve. Since $f \approx f_0$ in the polar region, the smooth curve has $\zeta \approx 0$ in this region. Up to latitude −85° the measured $\bar{u}$ increases slightly more steeply than the constant $\zeta + f$ curve. Poleward of −85° latitude $\bar{u}$ increases more slowly than the constant $\zeta + f$ curve, which may be

due to the turbulent frictional losses. Constant absolute vorticity is consistent with horizontal stirring by eddies. To explain the steeper curve outside the −85° region, some other mechanism could interfere with the eddy stirring. A curve steeper than the one for constant absolute vorticity may be produced for example by rings of air moving poleward, which would produce a profile with constant angular momentum. However this would be a much steeper curve than the data in Fig. 2A. Instead, angular momentum in the data decreases toward the center. The combination of eddy stirring and poleward motion may produce the observed wind profile.

We measured the meridional component of the clouds' motion which turned out to be undetectable within the errors for all the clouds except the ones in the inner eye. The clouds in the inner eye display a small radial motion, both inward and outward, in addition to their much larger zonal motion.

The multiple-filter observations probing different cloud altitudes are repeated four times during the 3 hours (see also Dyudina et al., 2008). False-color images are composed from the images taken with filters CB2, MT2, and MT3 (see Porco et al., 2004 for Cassini filter details). The four-frame color supplementary online movie 2combined from these false-color images shows that the clouds at different heights move at the same velocities. We estimate the cloud heights using methane gas absorption. The continuum narrow band filter CB2 (750 nm, red color plane) senses clouds and aerosols from the top of the atmosphere down to the deepest levels of the troposphere. The filter at weak methane absorption band MT2 (727 nm, green color plane) senses down to the intermediate depths. The exact values of the atmospheric pressure where the methane absorption reaches optical depth one for each wavelengths are usually derived from radiative transfer models and are somewhat model-dependent. Here we assume the penetration depths described in Tomasko et al. (1984). According to that model, at 727 nm the gaseous absorption optical depth one occurs at 1.2 bars at nadir viewing for a cloud-free atmosphere. At slant viewing (the images are observed at around 40° from horizon) the optical depth one occurs near 800 mbar. The effect of slant illumination is even more drastic than the effect of slant viewing. For the images composing the movie the Sun is 15.5° above the horizon at the pole. This translates into optical depth one for cloud-free atmosphere at ∼300 mbars, which would be further reduced by haze or cloud shadowing. The illumination angle changes considerably across the image, and so does the depth of the solar light penetration. The filter at the strong methane absorption band MT3 (889 nm, blue color plane) senses the highest part of the atmosphere. At this wavelength the absorption optical depth one occurs at 330 mbars for nadir viewing, which corresponds to 200 mbars for slant viewing, or to 80 mbars for solar illumination. For such a complex system the exact cloud heights can only be derived from a thorough radiative transfer model. Such a retrieval would be uncertain with the ISS data only and would greatly benefit from combining the ISS data with near-infrared and infrared data from Cassini VIMS and CIRS. The accurate cloud height retrieval is out of scope of this paper. However we can give a qualitative estimate of the relative cloud heights in movie 2with low clouds appearing red and high thin clouds appearing blue and green. The wind speeds are coherent at all elevations whenever small clouds are available for tracking. It should be noted though that inside −84° latitude only the deepest-probing red color plane clouds are suitable for tracking. In this region near the eye it is impossible to tell if the wind speeds are the same at all heights. The oval shape of the inner eye rotates coherently in all colors. It is unclear if it follows the wind field or not: it could be a wave that propagates relative to the fluid.

The deep red clouds are not seen with the methane absorption filters (MT2, which probes no deeper than 300 mbar, or MT3, which probes no deeper than 80 mbar, as discussed above). This agrees with the radiative transfer modeling conclusion by Sánchez-Lavega et al. (2006) who derive that the dense cloud tops displaying the vortex rotation in 2004 are located at 300–500 mbar.

4. Vorticity

For an oblate spheroid the absolute vorticity of the zonal flow can be written as

$$\zeta = \frac{1}{Rr}\frac{d}{d\varphi}(r\bar{u})$$

where R is the radius of curvature in the latitudinal direction, r is the radius of curvature in the zonal direction, and φ is the planetographic latitude. Planetographic latitude φ can be converted from planetocentric latitude ϕ using equatorial and polar radii R_e and R_p, and their ratio $\epsilon = R_e/R_p$:

$$\varphi = \arctan\left(\epsilon^2 \tan(\phi)\right).$$

Radii of curvature can be expressed as follows (Dowling and Ingersoll, 1989):

$$r(\varphi) = \frac{R_e}{(1+\epsilon^{-2}\tan^2\varphi)^{1/2}},$$

$$R(\varphi) = \frac{R_e}{\epsilon^2}\left(\frac{r}{R_e\cos\varphi}\right)^3.$$

The equation $\zeta + f = \text{constant}$, which was used in Fig. 2A, can be written in the notation of R and r, assuming $\zeta = 0$ and $\bar{u} = 0$ at $\varphi_0 = \arctan(\epsilon^2\tan(\phi_0))$:

$$\zeta + f = \frac{1}{Rr}\frac{d}{d\varphi}(r\bar{u}) + 2\Omega\sin\varphi = 2\Omega\sin\varphi_0.$$

The velocity curve for Fig. 2A is the result of numerical integration of the same equation rewritten as

$$\bar{u} = \frac{2\Omega R_e}{\epsilon^2}(1+\epsilon^{-2}\tan^2\varphi)^{1/2}\int_{\varphi_0}^{\varphi}\frac{(\sin\varphi_0 - \sin\varphi)\,d\varphi}{(1+\epsilon^{-2}\tan^2\varphi)^2\cos^2\varphi}.$$

The solid curve for the vorticity in Fig. 2B is a finite-difference version of the vorticity equation at the beginning of this section. For each pair of consecutive points in the spline curve fitted to the points from Fig. 2A (the spline curve is not shown in the plot) the vorticity is calculated as follows:

$$\zeta \approx \frac{4(r_1\bar{u}_1 - r_2\bar{u}_2)}{(r_1+r_2)(R_1+R_2)(\varphi_1-\varphi_2)}$$

where the subscripts correspond to the first and second point in the pair.

Multiple smaller clouds around the cyclone's eye (see Fig. 1) show detectable individual rotation. To determine the relative vorticity ζ of a cloud, we track it over the 3-hour time interval and measure its angular velocity of rotation relative to the rotating planet. Twice this angular velocity is the vorticity of the cloud. The angular velocity was obtained by a procedure similar to the manual feature tracking used for the zonal windspeeds, which involves picking an appropriate stopped motion movie from the set of test movies. To obtain each cloud's angular velocity we first determined its drift around the pole (see the technique described in Section 3). Then we made an individual cloud's movie from the set of 14 maps such that the movie frames track the cloud in its motion around the pole. Finally we made a set of modified back-rotated movies from these cloud-centered frames for a set of test angular velocities. While simultaneously playing the set of back-rotated movies we picked the one that stopped the apparent rotation of the cloud. Because individual clouds are not always covered by all 14 images, some modified movies have less than 14 time steps, down to as

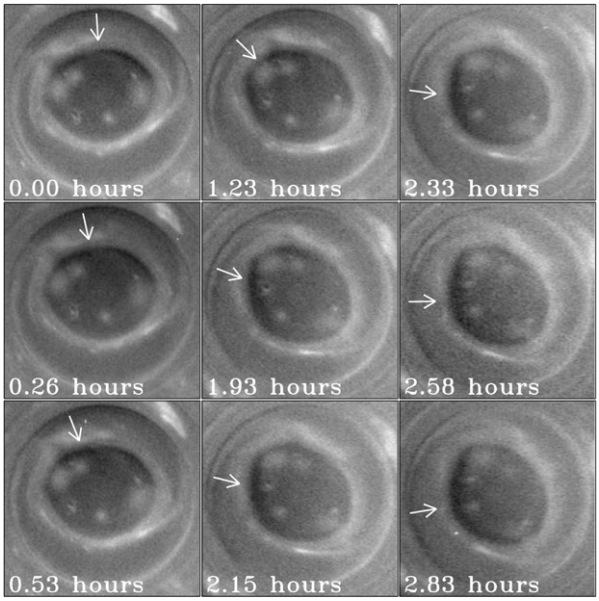

Fig. 3. A set of the maps showing how the shadow of the cyclone's eyewall follows the Sun. The diffuse dark band inside each of the two eyewalls is a shadow cast by the eyewall on the clouds inside the eye. The first map is taken on October 11 (DOY 284), 2006 at 19 h 42 min 31 s. The time on the maps increases from top to bottom panel and then from left to right, as labeled by the time in hours from the start of the sequence. The white arrow on each panel shows the direction at which the Sun illuminates the planet. The arrow points from the Sun to the illuminated scene.

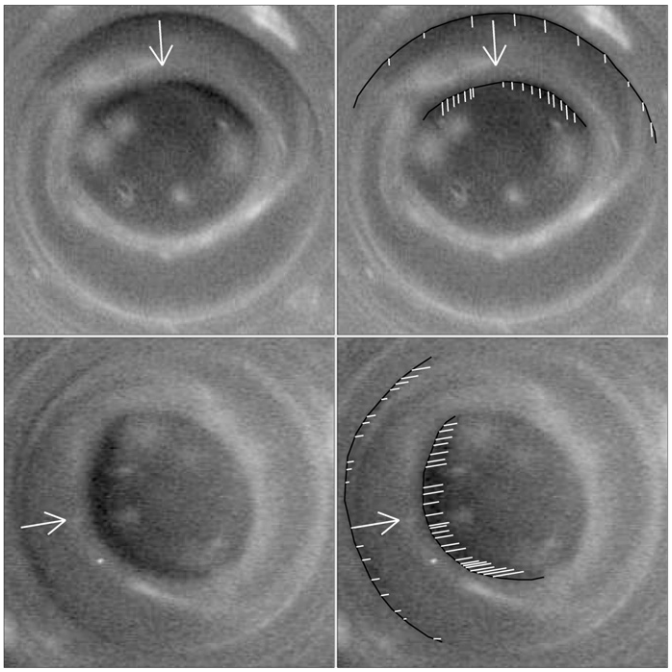

Fig. 4. Two maps demonstrating how the length of the shadows had been estimated. The left panels show the map, the right panels show the same map with the cyclone eyewalls outlined in black and shadow lengths measured on this image shown in white.

few as 2 time steps, which creates additional uncertainty. Often it is uncertain which of the movies matches the rotation of the cloud. To test the uncertainty and to increase the precision of the vorticity measurements we measured vorticity of each cloud 3–4 times, picking the range of reasonably good matches. The vorticity values (colors of the asterisks in Fig. 1 and points in Fig. 2B) are the averages of those 3–4 measurements. The error bars are calculated as a standard deviation of the measurements. Nearly all small clouds rotate counterclockwise (anticyclonic vorticity). The largest features (the two dark spots at the upper left corner of the map in Fig. 1) rotate the fastest. For the smaller clouds the relation between the size and rotation is not systematic.

5. Eyewall heights

The cyclone's eyewalls are steep and cast shadows on the lower clouds inside the eye. Fig. 3 shows that the dark crescent-shaped areas inside the walls follow the Sun in a counterclockwise direction as the planet turns during the 3-hour period. This demonstrates that the dark areas are indeed shadows and not a dark coloration of the underlying clouds.

Fig. 4 shows how we derived the height of the eyewalls above the main cloud layer inside the eye from the length of the shadows (see also the brief estimate of eyewall heights in Dyudina et al., 2008). The two maps in the figure are examples of the nine maps from Fig. 3, which we used for the eyewall height calculation. We manually picked the points of the apparent end of the shadow and projected these points along the Sun's azimuth to the edge of the eyewall. The reader may judge the uncertainty by comparing the left panels of Fig. 4 with the right panels, which show the same maps overlaid with our estimated shadow locations. We assumed the clouds inside the eye are flat and horizontal. To obtain the eyewall height we multiplied each shadow length by the tangent of the solar elevation angle above the horizon, which is around 16° for the inner eyewall and 17° for the outer eyewall for all the images (as the Sun is 15° above the horizon at the pole and the eyewalls are 1° and 2° away from the pole).

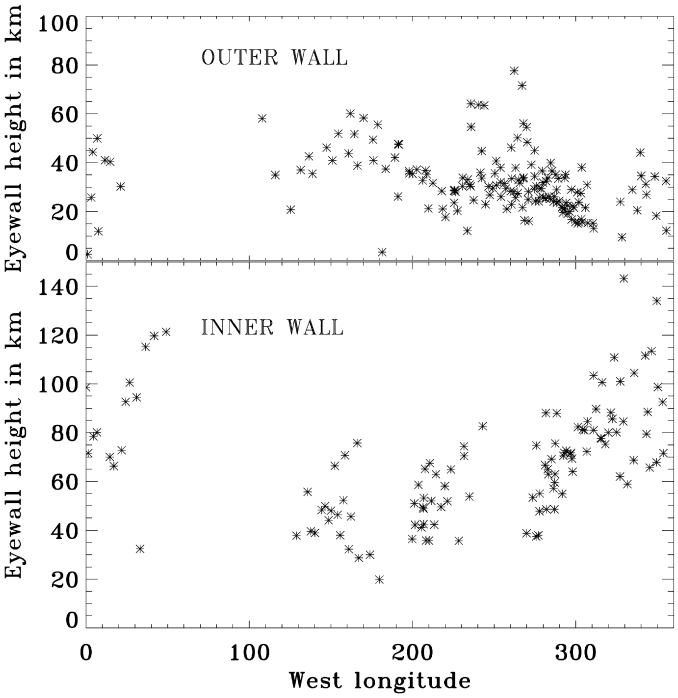

Fig. 5. Height of the outer (upper panel) and inner (lower panel) walls of the vortex. The height is plotted versus longitude of the wall features in the first image of the sequence (first panel in Fig. 3, or upper panel of Fig. 4). The shadow lengths are taken from all images from Fig. 3. Then the longitude of the points on the wall casting the measured shadows is adjusted to account for the zonal velocity of the wall. The zonal velocities are 17 degrees/h and 20 degrees/h for the outer and inner walls respectively.

Fig. 5 shows the resulting heights for outer and inner eyewalls calculated from the nine maps. The data are plotted versus the longitude where each shadow point projects to the eyewall. The longitudes are adjusted (rotated back) to account for the rotation

of the eyewall. With such an adjustment the shadows of particular eyewall features (e.g., the "bulge" of the inner wall oval) appear at the same longitude for all images. We assumed zero adjustment for the first image in Fig. 3, which is also the image in the upper panel of Fig. 4. The height of the outer wall is about 30–40 km and does not significantly change with longitude. The height of the inner wall depends significantly on longitude. At longitude ~180° the shadows are shorter and the corresponding wall height is ~30–60 km. Shorter shadows can be seen in the upper image in Fig. 4, which is taken at the time when the Sun illuminated the image from longitude ~180° (up on the map). The Sun proceeds to larger longitudes of 350°–50° with time. The last frame in the time sequence is shown in the lower panels of Fig. 4. The shadows are longer at those longitudes and the corresponding wall heights are ~70–120 km. Both the upper and lower image probe the shadows on the long sides of the inner eye's ellipse. The eyewall on one long side is taller than that on the opposite long side. On the short side of the ellipse (longitude ~270°) the shadow lengths are nearly impossible to measure because of the bright clouds inside the eye.

The height of the inner wall (70 ± 30 km) is about twice the pressure scale height (vertical e-folding distance) of Saturn's atmosphere. The eyewalls are consistent with rising motion above a deeper cloud layer, since clouds form on updrafts.

Because the cloud wall is visible in the MT3 images sensitive to the highest clouds (see Section 3) it appears that the eyewall clouds extend above the tropopause, which is at the ~100 mbar level (see Section 6).

6. Thermal data from Cassini CIRS

The temperature distribution with latitude and height in the left panel of Fig. 6 is derived from Cassini/CIRS spectra (Flasar et al., 2004; Irwin et al., 2008; Fletcher et al., 2008) taken on July 30, 2005 from an orbital distance of 28 Saturn radii. Tropospheric zonal mean temperatures in the 70–800 mbar region (bottom left) and stratospheric zonal mean temperatures between 1–6 mbar (top left) are derived from the 600–1400 cm^{-1} region of CIRS mid-IR spectra. The temperature information originates from fits to the ν_4 CH_4 band and the H_2–He collision-induced continuum at 15.0 cm^{-1} spectral resolution (Irwin et al., 2008). The temperature minimum at ~100 mbar indicates the tropopause.

The right panels of Fig. 6 show the hot temperature anomaly at the pole relative to the temperatures at same pressure levels away from the pole. The anomaly coincides with the SPV eye (marked by dashed vertical lines in Fig. 6). The anomaly reaches values of more than 5 K immediately below and above the 100-mbar tropopause.

Fig. 7 is derived from Cassini/CIRS data taken on October 11, 2006 from an orbital distance of 5.6 Saturn radii simultaneously with the visible images discussed in this paper. It shows the temperatures at the 100-mbar level (Flasar et al., 2004). This is near the tropopause, and it shows the concentration of warm air inside the outer eyewall. The gases near the pole are ~4 K warmer than their surroundings. The scanning pattern did not cover the pole itself. This 2006 warm core is consistent with the 2005 warm core in Fig. 6 and with the warm core observed by CIRS in 2007 (Fletcher et al., 2008). The thermal anomaly has been present since it was discovered in 2003 (Orton and Yanamandra-Fisher, 2005). The visible structure of the eye has been present at least since 2004 (Vasavada et al., 2006; Sánchez-Lavega et al., 2006), which shows the stability of the cyclone's motion as well as the stability of the warm core.

The 100-mbar and 200-mbar temperature maps in Fig. 7 are taken by CIRS simultaneously with October 11, 2006 ISS images. They show the hot anomaly at the pole of about the same strength as in 2005. The temperature anomaly is about 1 K stronger at 100 mbar (left panel of Fig. 7) than at 200 mbar (right panel

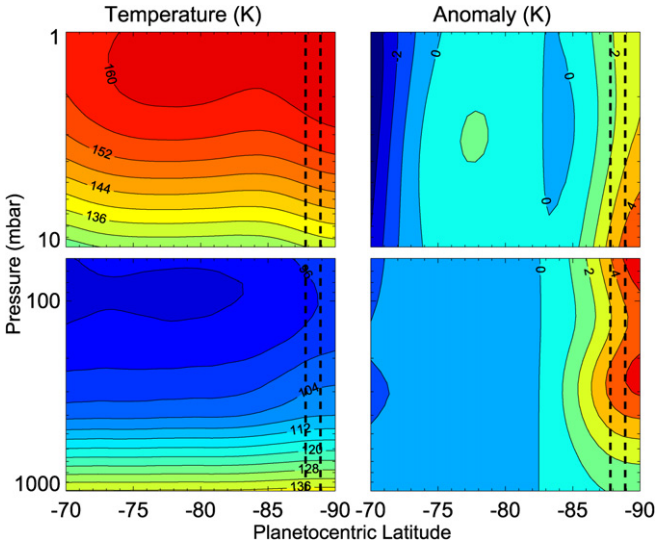

Fig. 6. Zonal mean temperatures in Saturn's south polar region derived from Cassini CIRS spectra (left panels) (Fletcher et al., 2008; Flasar et al., 2004; Irwin et al., 2008). The gap between the upper and lower panels arises because the CIRS instrument is not sensitive to the 6–70 mbar region. Temperature anomalies (right panels) are calculated by subtracting the zonal mean temperatures at −84° latitude. The dashed vertical lines indicate the inner and outer eyewalls.

of Fig. 7, note a different temperature scale). The stronger 100-mbar anomaly in high-resolution mapping in 2006 is unexpected because in the 2005 low-resolution data (Fig. 6) the anomaly is stronger at 200 mbar. This disagreement is probably due to lower spatial and spectral resolution of the 2005 data, though it may be a real temporal change in the warm core. Both 100-mbar and 200-mbar maps show azimuthal asymmetry of the warm core. This azimuthal asymmetry has no obvious relation with the oblong shape of the cyclone's inner eye (see the ISS image at a background) or with the small clouds within the eye. However some caution should be taken when comparing different parts of the Fig. 7 maps. Because of the planet's curvature and the slant viewing, different points on the maps are observed at different emission angles, and this can lead to different altitudes (and therefore different temperatures) being sounded.

The meridional thermal gradient in the warm core is expected to weaken the cyclonic circulation with altitude. For example, the circulation would weaken due to the thermal wind at the inner eyewall (−89° latitude) by ~10 m/s as the altitude changes from 400 mbar to 80 mbar. The circulation weakening for the outer parts of the cyclone would be smaller because of the smaller thermal gradients there. Such weakening is undetectable within the error bars of our wind measurements (see Fig. 2A). Because of that the conclusion about non-balanced flow in the cyclone proposed by Dyudina et al. (2008) is misleading. Instead of indication of non-balanced flow, the non-detection of the circulation weakening is likely due to the uncertainty in our wind measurements.

The warm core may be due to a local subsidence in the atmosphere, which would create the dry cloud-free conditions observed in the visible ISS images.

7. Winds observed in 5-micron emission by Cassini VIMS

Cassini VIMS observed Saturn in both reflected solar light and in thermal emission from Saturn. Fig. 8 shows the map-projected mosaic of the VIMS images taken in thermal emission wavelength of 5.12 microns at the same time as the ISS and CIRS maps from Figs. 1 and 7. Dense clouds block thermal emission and show up in silhouette as dark spots in the images. Since the south polar area

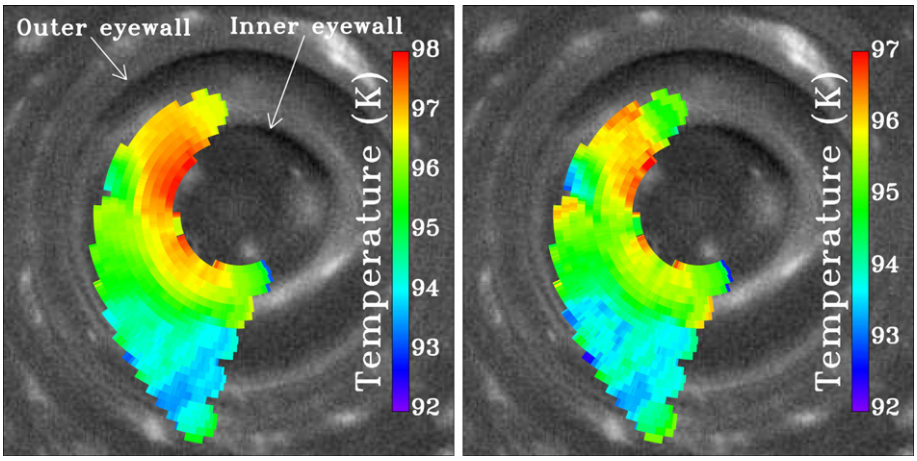

Fig. 7. Temperature map at the 100-mbar level (left panel) and temperature map at the 200-mbar level (right panel) derived from the Cassini CIRS (Flasar et al., 2004) observations taken on October 11, 2006 at spatial resolution of ~100 km/pixel. The temperature is shown in color. Note different temperature color scales for the left and right panels. The grayscale ISS 750-nm image at the background had been taken simultaneously with the temperature map. (For interpretation of the references to color in this figure legend, the reader is referred to the web version of this article.)

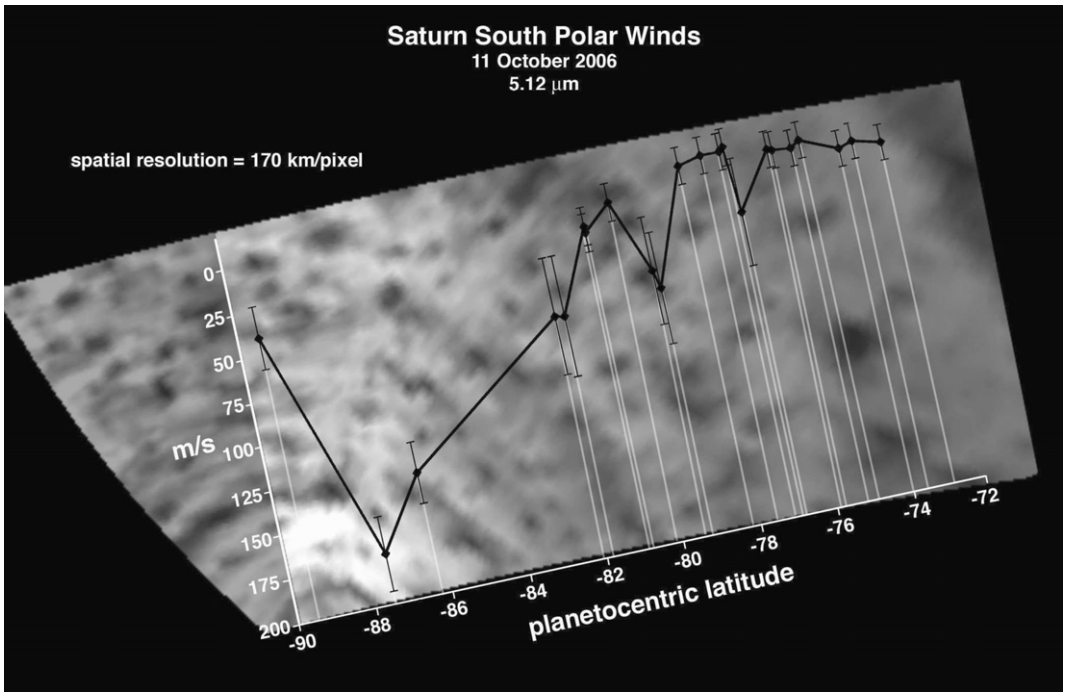

Fig. 8. A diagram that shows VIMS zonal winds overlying an image mosaic of the south pole of Saturn. The pole is in the lower left. The dark spots are the clouds arranged in circular bands around the pole. The abscissa of the wind plot shows the latitudes as they project on the map. Note that the winds are "inverted", with the ordinate showing large winds at the bottom and small winds at the top.

is lighted by the Sun, which interferes with interpreting the thermal emission, it is hard to estimate the exact altitudes of these clouds. But we believe these clouds are in the ~1–2.5-bar region based on spectral analysis of darkside images which indicate ~2 bars (on average) there, assuming that phosphine does not change radically from latitude to latitude across the planet. The large disparity in the appearance of features seen by VIMS in silhouette at 5-micron versus those seen in reflected light gives credence that we are looking at lower levels than usually seen. In the south polar region, there is a much stronger correlation between visible reflective and near-IR thermal silhouette images, which indicates significantly less haze opacity there than elsewhere on the planet. This deeper atmosphere view in reflected light is supported by VIMS analysis of ammonia and phosphine column abundances as well as methane band imagery, all of which are consistent with seeing significantly deeper there than elsewhere on the planet (as noted in Baines et al., 2005).

The map in Fig. 8 is overlaid by the zonal winds derived from the VIMS images. We tracked the 5-micron winds by following dark clouds over a 2 h 40 min period on October 11, 2006. To get zonal winds we fit a slope to the observed longitudes changing over time. Each longitude has an error bar associated with it that is ±1/2 a ~170-km-wide VIMS pixel. We do a linear fit to the points with a Bevington-based linear fitting routine which also produces the standard deviation of the slope, which we take as an error bar. Most latitudes have just one measurement, but a few had two measurements. We show the average of the two measurements and the net error bar.

Table 1
Comparison of the Saturn south polar vortex (SPV) with terrestrial hurricanes (Anthes, 1982; Emanuel, 2003), terrestrial Arctic and Antarctic polar vortices on Earth (PV Earth) (Holton, 2004), Jupiter's Great Red Spot (GRS) (Vasavada and Showman, 2005), south polar vortex on Venus (PV Venus) (Piccioni et al., 2007), and the warm spot at the south pole of Neptune (Orton et al., 2007). The "diameter" refers to the major axis of the area enclosed within the maximum winds. For the SPV and terrestrial hurricanes, this is the diameter of the eye. The temperature anomaly refers to the atmospheric level where observable clouds are located. The anomaly may have different sign higher or lower in the atmosphere. The "unknown" eyewall clouds may be blocked from the view by higher clouds. The vorticity ratio ζ/f is effectively the Rossby number R_0.

Parameter of comparison	SPV	Hurricane	PV Venus	PV Earth	GRS	Neptune pole
Diameter (km)	4200	20–100	2700	1000–2000	10000–40000	<7000
Diameter (% of the planet's radius)	7	0.3–1.5	45	15–30	14–56	<25
Lifetime	>4 years	weeks	years	seasonal	>150 years	unknown
Max. windspeeds ($m\,s^{-1}$)	150	85	35	50	120–190	unknown
Temperature anomaly	warm	warm	warm	cold	cold	warm
Sense of rotation	cyclonic	cyclonic	cyclonic	cyclonic	anticyclonic	unknown
Eyewall clouds	yes	yes	unknown	no	unknown	unknown
Fixed polar location	yes	no	yes	yes	no	yes
Convective clouds on periphery	yes	yes	no	no	yes	unknown
Bounded by rigid surface	no	yes	no	yes	no	no
$\zeta/f \sim R_0$	1	100	100	1	−0.2	unknown

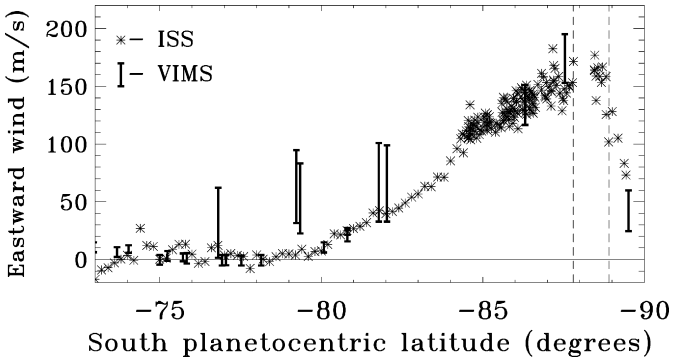

Fig. 9. Comparison of zonal velocity (eastward) measured by ISS in CB2 filter (asterisks) with velocity measured by VIMS in 5.12 microns (error-bar-style points). The dashed vertical lines indicate the inner and outer eyewalls.

Fig. 9 shows that the VIMS winds measured above 1–2.5 bars generally agree with the ISS winds measured at similar or higher altitudes with CB2 (750 nm) filter, which probes deeper than ~300 mbar, see Section 3. Near the eyewalls clouds are seen by ISS and VIMS at the same locations. This may indicate either that VIMS and ISS are sensing similar altitudes, or that these clouds are extended vertically. In the case of vertically extended clouds ISS sees the cloud tops, and VIMS sees the integrated opacity of the cloud above 2.5 bar level.

A group of VIMS data points may indicate stronger winds at depth. The large-error data points between latitudes −76° and −83° show much higher speeds of 40–80 m/s than the VIMS points having small error at the same latitudes, for which values are below 20 m/s. The small-error VIMS points are in perfect agreement with ISS observations, and probably result from tracking the same clouds as ISS at similar altitudes. The 40–80 m/s points may be tracking deeper clouds not visible to ISS, which then are much faster than the <10 m/s winds expected from a thermal wind balance at these latitudes (see Section 6).

8. Comparison with vortices on other planets

Table 1 shows a comparison of the SPV with other vortices in the Solar System.

The role of the planetary rotation for the vortices is given by the value of ζ/f, or the Rossby number R_0. The various vortices divide up into 3 classes: high R_0 phenomena in which planet rotation is completely a secondary consideration due either to small spatial scale (hurricanes) or slow rotation (Venus), low R_0 phenomena (GRS) which are quasi-geostrophic and more dynamically similar to synoptic scale anticyclones on Earth, and then the SPV and terrestrial polar vortex, which rotate at a rate comparable to the planet's.

For detailed comparison of GRS on Jupiter with terrestrial hurricanes we refer the reader to Flasar et al. (1981) and Ingersoll (1976). We did not show the north polar vortex on Venus (Taylor et al., 1979), which is similar to the one at the south (Piccioni et al., 2007).

Terrestrial hurricanes and the Venus polar vortex show the most similarities to the SPV, such as cyclonic rotation, warm temperature anomaly, cloudy eyewalls in the case of hurricane, and polar location in the case of the Venus polar vortex.

Because much more is known about terrestrial hurricanes than about the Venus polar vortices, we compare SPV to the hurricane in more detail. A hurricane (typhoon, tropical cyclone) is a warm-core vortex sustained by enthalpy fluxes across the air–sea interface when in-flowing air in the boundary layer picks up water vapor from the ocean (Palmen and Newton, 1969; Anthes, 1982; Emanuel, 2003). Saturn and the other giant planets do not have oceans to supply water. They also do not have any other boundary to restrict vertical air motion. However, giant planets do have deep, moisture-laden atmospheres below the clouds which may interact with dry upper atmosphere providing driving force for the vortex. The strength of this interaction should depend on the poorly known water abundance in the planets' interior and whether upward turbulent mixing of water vapor into the cloud-forming region is enhanced at latitudes where the zonal winds are strongest.

A hurricane has a central low pressure at low altitudes. The radial pressure gradient becomes weaker at high altitudes because of the lower density of the warm air at the center. No direct measurements of altitude can be done for Saturn's polar vortex to compare with this pressure pattern, but it is expected there due to the warm core.

Condensation and release of latent heat are greatest in a ring of clouds surrounding the central eye, which is sometimes clear and sometimes partly cloud covered. The eye of the SPV is clear at high elevations with a few deep clouds in it. The eyewall clouds of the hurricane tower two scale heights (vertical e-folding distance), about 15 km, above the surface. The SPV inner eyewall is 30–70 km tall, which is also about twice the scale height.

Hurricanes dissipate quickly when they leave the ocean and run over land. Saturn has no land, vortices usually live longer, and as of September 2008 the SPV is still observed by Cassini, which shows that it is at least four years old, and possibly permanent.

The central eye of the hurricane, typically 20–100 km in diameter, is warmer than its surroundings to the height of the tropical tropopause, and has a cold anomaly above the tropopause. The strongest warm core indicates the layer of outflow just below the tropopause (Emanuel, 2003). SPV has a warm anomaly extend-

ing from below to above the tropopause, which may be due to the radiative heating from the long-lived warm core below. The strongest warm cores of the SPV are immediately below and above the tropopause (see Fig. 6).

Sometimes hurricanes have multiple concentric eyewalls which contract with time and get replaced by the outer walls on the timescale of days (Houze et al., 2007). SPV's two walls are seen throughout the four years of observations.

In a hurricane the winds are greatest in the eyewall and can reach speeds of 85 $m\,s^{-1}$. In SPV the winds are also greatest in the eyewall. The peak winds are 150 ± 20 $m\,s^{-1}$, about twice those of a terrestrial hurricane.

In both hurricane and SPV the relative vorticity ζ is large in the eye out to the eyewall and small in the region beyond, where the tangential velocity decays to zero (see Fig. 2). The vorticity at the center of a hurricane is cyclonic – clockwise in the southern hemisphere and counterclockwise in the northern hemisphere. SPV is also cyclonic.

The angular momentum in hurricanes decreases toward the center, as in the SPV (see discussion of Fig. 2 in Section 3). On Earth, rings of air flowing inward lose angular momentum to the lower boundary and to the outflowing air above (Palmen and Newton, 1969; Anthes, 1982; Emanuel, 2003). On Saturn the inflow is not directly measured, but a slow inflow may exist (see the discussion of radial wind profile in Section 3). On Saturn there is no lower boundary, and it is possible that deep winds are as strong as the winds at the observable level (see Section 7). The possible outflowing air above the SPV and stirring by the eddies may act as a sink for angular momentum similar to the hurricanes.

Hurricanes are usually surrounded by heavily precipitating clouds. In this respect the small bright clouds around the eye of the SPV (see Fig. 1) are like the rain bands of a terrestrial hurricane, though rain bands usually form spirals around the hurricane, which is not the case for the small bright clouds. However annular hurricanes (Knaff et al., 2003), which are long-lived and symmetric terrestrial hurricanes that form in an unusually calm background atmosphere, do not show spiral rain bands and are probably more similar to the polar vortex on Saturn.

Many smaller vortices on Jupiter and Saturn have circular shapes and sharp boundaries, which may resemble the eye structure of the polar vortex. However the insufficient spatial resolution of available images prevents the determination of cloud walls or strong winds around those vortices. An interesting example of convective clouds that erupt and then develop into circular dark spots on the timescales of several days are the thunderstorms at the 35° S on Saturn (Dyudina et al., 2007).

Hurricanes, the Venus polar vortex, and other big planetary vortices in Table 1 display some similarity to the SPV, but there are also differences, and no close analogue to SPV can be confidently determined.

The hot polar spot on Neptune's south polar region, recently discovered by Orton et al. (2007), may potentially be such an analogue. Atmospheric motion at the pole of Neptune could be similar to Saturn's because it is also a giant planet with a deep atmosphere. Although Orton et al. (2007) argue that the hot spot in Neptune's troposphere may be due to the seasonal heating (it is in mid-summer now), the vortex like SPV would also explain the hot spot.

Cassini CIRS measurements show a similar hot spot at the north pole of Saturn (Fletcher et al., 2008). Cassini/VIMS recently observed a vortex at the north pole which has similar winds as that at the south (Baines et al., 2009), though the cloud morphology of the northern hemisphere is somewhat different from the southern hemisphere. The seasonal heating would not explain this hot spot because the north pole is now in winter. Saturn's northern hot spot is also a region of depleted PH3, similar to the eye of SPV, suggestive of atmospheric subsidence (Fletcher et al., 2008). Cassini camera will be able to observe the north vortex when the north pole becomes illuminated by the Sun after the August 11, 2009 equinox.

It is possible that all giant planets have polar vortices but the observations are so far insufficient for detection. The south pole of Saturn is the first pole of a giant planet observed at adequate spatial resolution to track the clouds. More Cassini observations will cover both Saturn's poles. For Jupiter, a spacecraft in a high-inclination orbit (such as Juno scheduled to arrive to Jupiter in 2016) would be needed to observe winds at the poles. More high-inclination space missions would be needed to observe winds at the poles of Uranus and Neptune.

Acknowledgment

This research was supported by the NASA Cassini Project.

Supplementary material

The online version of this article contains additional supplementary material.

Please visit DOI: 10.1016/j.icarus.2009.02.014.

References

Anthes, R.A., 1982. Tropical Cyclones. Their Evolution, Structure and Effects. American Meteorological Society.

Baines, K.H., Drossart, P., Momary, T.W., Formisano, V., Griffith, C., Bellucci, G., Bibring, J.P., Brown, R.H., Buratti, B.J., Capaccioni, F., Cerroni, P., Clark, R.N., Coradini, A., Combes, M., Cruikshank, D.P., Jaumann, R., Langevin, Y., Matson, D.L., McCord, T.B., Mennella, V., Nelson, R.M., Nicholson, P.D., Sicardy, B., Sotin, C., 2005. The atmospheres of Saturn and Titan in the near-infrared first results of Cassini/VIMS. Earth Moon Planets 96, 119–147.

Baines, K.H., Momary, T.W., Fletcher, L.N., Showman, A.P., Roos-Serote, M., Brown, R.H., Buratti, B.J., Clark, R.N., 2009. Saturn's north polar cyclone and hexagon at depth revealed by Cassini/VIMS. Planet. Space Sci., submitted for publication.

Desch, M.D., Kaiser, M.L., 1981. Voyager measurement of the rotation period of Saturn's magnetic field. Geophys. Res. Lett. 8, 253–256.

Dowling, T.E., Ingersoll, A.P., 1989. Jupiter's Great Red Spot as a shallow water system. J. Atmos. Sci. 46, 3256–3278.

Dyudina, U.A., Ingersoll, A.P., Ewald, S., Vasavada, A., West, R.A., Del Genio, A., Barbara, J., Porco, C.C., Achterberg, R., Flasar, F., Simon-Miller, A., Fletcher, L., 2008. Dynamics of Saturn's south polar vortex. Science 319, 1801.

Dyudina, U.A., Ingersoll, A.P., Ewald, S.P., Porco, C.C., Fischer, G., Kurth, W., Desch, M., Del Genio, A., Barbara, J., Ferrier, J., 2007. Lightning storms on Saturn observed by Cassini ISS and RPWS during 2004–2006. Icarus 190, 545–555.

Emanuel, K., 2003. Tropical cyclones. Annu. Rev. Earth Planet. Sci. 31, 75–104.

Flasar, F.M., Conrath, B.J., Pirraglia, J., Clark, P.C., French, R.G., Gierasch, P.J., 1981. Thermal structure and dynamics of the jovian atmosphere. I. The Great Red Spot. J. Geophys. Res. 86, 8759–8767.

Flasar, F.M., Kunde, V.G., Abbas, M.M., Achterberg, R.K., Ade, P., Barucci, A., Bézard, B., Bjoraker, G.L., Brasunas, J.C., Calcutt, S., Carlson, R., Césarsky, C.J., Conrath, B.J., Coradini, A., Courtin, R., Coustenis, A., Edberg, S., Edgington, S., Ferrari, C., Fouchet, T., Gautier, D., Gierasch, P.J., Grossman, K., Irwin, P., Jennings, D.E., Lellouch, E., Mamoutkine, A.A., Marten, A., Meyer, J.P., Nixon, C.A., Orton, G.S., Owen, T.C., Pearl, J.C., Prangé, R., Raulin, F., Read, P.L., Romani, P.N., Samuelson, R.E., Segura, M.E., Showalter, M.R., Simon-Miller, A.A., Smith, M.D., Spencer, J.R., Spilker, L.J., Taylor, F.W., 2004. Exploring the Saturn system in the thermal infrared: The composite infrared spectrometer. Space Sci. Rev. 115, 169–297.

Fletcher, L.N., Irwin, P.G.J., Orton, G.S., Teanby, N.A., Achterberg, R.K., Bjoraker, G.L., Read, P.L., Simon-Miller, A.A., Howett, C., de Kok, R., Bowles, N., Calcutt, S.B., Hesman, B., Flasar, F.M., 2008. Temperature and composition of Saturn's polar hot spots and hexagon. Science 319, 79–82.

Holton, J.R., 2004. An Introduction to Dynamic Meteorology, 4th ed. Elsevier Academic Press, Amsterdam.

Houze, R.A., Chen, S.S., Smull, B.F., Lee, W.-C., Bell, M.M., 2007. Hurricane intensity and eyewall replacement. Science 315, 1235–1239.

Ingersoll, A.P., 1976. The atmosphere of Jupiter. Space Sci. Rev. 18, 603–639.

Irwin, P.G.J., Teanby, N.A., de Kok, R., Fletcher, L.N., Howett, C.J.A., Tsang, C., Wilson, C., Calcutt, S.B., Nixon, C.A., Parrish, P., 2008. The NEMESIS planetary atmosphere radiative transfer and retrieval tool. J. Quant. Spectrosc. Radiat. Trans. 109 (6), 1136–1150.

Knaff, J.A., Kossin, J.P., DeMaria, M., 2003. Annular hurricanes. Weather Forecasting 18, 204–223.

Orton, G.S., Encrenaz, T., Leyrat, C., Puetter, R., Friedson, A.J., 2007. Evidence for methane escape and strong seasonal and dynamical perturbations of Neptune's atmospheric temperatures. Astron. Astrophys. 473, L5–L8.

Orton, G.S., Yanamandra-Fisher, P.A., 2005. Saturn's temperature field from high-resolution middle-infrared imaging. Science 307, 696–698.

Palmen, E., Newton, C.W., 1969. Atmospheric Circulation Systems. Academic Press, New York, London.

Piccioni, G., Drossart, P., Sanchez-Lavega, A., Hueso, R., Taylor, F., Wilson, C., Grassi, D., Zasova, L., Moriconi, M., Adriani, A., Lebonnois, S., Coradini, A., Bézard, B., Angrilli, F., Arnold, G., Baines, K.H., Bellucci, G., Benkhoff, J., Bibring, J.P., Blanco, A., Blecka, M.I., Carlson, R.W., Lellis, A.D., Encrenaz, T., Erard, S., Formisano, S.F., Fouchet, T., Garcia, R., Haus, R., Helbert, J., Ignatiev, N.I., Irwin, P., Langevin, Y., Lopez-Valverde, M.A., Luz, D., Marinangeli, L., Orofino, V., Rodin, A.V., Roos-Serote, M.C., Saggin, B., Stam, D.M., Titov, D., Visconti, G., Zambelli, M., the VIRTIS-Venus Express Technical Team, 2007. South-polar features on Venus similar to those near the north pole. Nature 450 (7170), 637–640.

Porco, C.C., West, R.A., Squyres, S., McEwen, A., Thomas, P., Murray, C.D., Delgenio, A., Ingersoll, A.P., Johnson, T.V., Neukum, G., Veverka, J., Dones, L., Brahic, A., Burns, J.A., Haemmerle, V., Knowles, B., Dawson, D., Roatsch, T., Beurle, K., Owen, W., 2004. Cassini imaging science: Instrument characteristics and anticipated scientific investigations at Saturn. Space Sci. Rev. 115, 363–497.

Sánchez-Lavega, A., Hueso, R., Pérez-Hoyos, S., Rojas, J.F., 2006. A strong vortex in Saturn's south pole. Icarus 184, 524–531.

Taylor, F.W., McCleese, D.J., Diner, D.J., 1979. Polar clearing in the Venus clouds observed from the pioneer orbiter. Nature 279, 613–614.

Tomasko, M.G., West, R.A., Orton, G.S., Teifel, V.G., 1984. Clouds and aerosols in Saturn's atmosphere. In: Gehrels, T., Matthews, M.S. (Eds.), Saturn. Univ. of Arizona Press, Tucson, AZ, pp. 150–194.

Vasavada, A.R., Hörst, S.M., Kennedy, M.R., Ingersoll, A.P., Porco, C.C., Del Genio, A.D., West, R.A., 2006. Cassini imaging of Saturn: Southern hemisphere winds and vortices. J. Geophys. Res. (Planets) 111, 5004–5017.

Vasavada, A.R., Showman, A.P., 2005. Jovian atmospheric dynamics: An update after Galileo and Cassini. Rep. Prog. Phys. 68, 1935–1996.